



Synchronous optical intensity and phase measurements to characterize Rayleigh–Bénard convection

NATHANIEL A. FERLIC,^{1,*} SVETLANA AVRAMOV-ZAMUROVIC,² OWEN O'MALLEY,²
K. PETER JUDD,³ AND LINDA J. MULLEN¹

¹Naval Air Warfare Center Aircraft Division, 22347 Cedar Point Road, Patuxent River, Maryland 20670, USA

²Weapons, Robotics, and Control Engineering Department, United States Naval Academy, 597 McNair Rd. Hopper Hall, Annapolis, Maryland 21402, USA

³United States Naval Research Laboratory, 4555 Overlook Ave. SW, Washington DC, 20375, USA

*nathaniel.a.ferlic.civ@us.navy.mil

Received 13 April 2023; revised 16 July 2023; accepted 20 July 2023; posted 20 July 2023; published 2 August 2023

Propagation of a laser beam through the Rayleigh–Bénard (RB) convection is experimentally investigated using synchronous optical wavefront and intensity measurements. Experimental results characterize the turbulence strength and length scales, which are used to inform numerical wave optic simulations employing phase screens. Experimentally found parameters are the refractive index structure constant, mean flow rate, kinetic and thermal dissipation rates, Kolmogorov microscale, outer scale, and shape of the refractive index power spectrum using known models. Synchronization of the wavefront and intensity measurements provide statistics of each metric at the same instance in time, allowing for two methods of comparison with numerical simulations. Numerical simulations prove to be within agreement of experimental and published results. Synchronized measurements provided more insight to develop reliable propagation models. It is determined that the RB test bed is applicable for simulating realistic undersea environments. © 2023 Optica Publishing Group

<https://doi.org/10.1364/JOSAA.492749>

1. INTRODUCTION

Investigation of underwater optical turbulence has gained significant interest due to the growth of applications using optical signals for imaging [1], communications [2], and sensing [3]. The ability to experimentally recreate oceanic conditions is a difficult task in the lab; therefore, simplified models of oceanic conditions can be implemented using confined turbulence in water tanks. Temperature-driven density gradients are a process in the ocean that is accessible to isolate in a laboratory setting by heating water from below, thus creating a process called Rayleigh–Bénard (RB) convection. A RB water tank contains a hot plate on the bottom and a cold plate on the surface separated by the distance L , called the characteristic length, with no disruptions in between. The RB model experimentally generates natural convection that is ubiquitously present in oceanic and atmospheric environments. These random temperature fluctuations induce changes in the water's refractive index and thus creates optical turbulence along the propagation path. Characterization of the RB convection provides the necessary insight on how to mitigate the effects of optical turbulence on laser light in any medium. Applications include free-space communications systems [2,4–7], sensor networks [1,3], and energy-delivery systems [8,9].

Quantification of RB convection is accomplished using the Rayleigh (Ra) and Prandtl (Pr) number

$$\text{Ra} = \frac{g\alpha_t \Delta T L^3}{\nu D_T}, \quad (1)$$

$$\text{Pr} = \nu / D_T, \quad (2)$$

where g [ms^{-2}] is gravity, α_t [K^{-1}] is water's thermal expansion coefficient, ΔT [K] is the temperature difference between the thermal sources, L [m] is characteristic length, $\nu = \mu / \rho$ [$\text{m}^2 \text{s}^{-1}$] is water's kinematic viscosity, D_T [$\text{m}^2 \text{s}^{-1}$] is the thermal diffusivity of water, μ is the fluid's dynamic viscosity, and ρ is the fluid density.

The Rayleigh number quantifies an overall “macroscale” behavior of the turbulence, whereas the Prandtl number is a fluid property representing the ratio of momentum to thermal diffusivity. The Prandtl number determines how viscosity of the fluid will affect how kinetic energy in a turbulent field dissipates [10,11]. Various studies have explored how underwater turbulence at varying Ra affects optical systems [1,12–22] and field studies obtaining oceanic turbulence data [3,23].

The available theoretical (Grossmann–Lohse [GL] theory [24–27]) treatment of confined RB convection provides a fluid

dynamics point of view that connects to optical turbulence properties. The study of light propagation through RB turbulence is ingrained within the refractive index power spectral density (PSD), whose effects can be observed using optical intensity and/or wavefront measurements. Measurement of the turbulence strength alone does not provide full insight into the impact of turbulence on light. Therefore, obtaining optical wavefront and intensity statistics simultaneously provides a significant amount of feedback in estimating turbulent length scales and fluctuation strengths otherwise not accessible. This method allows a unique opportunity to compare a laser's amplitude and phase statistics to numerical simulation. Characterization of RB convection using synchronous measurements has not been experimentally performed [1,12–22]. Wave optic simulations (WOS) have been previously used to model angle-of-arrival fluctuations and beam wander with experimental confirmation [15]. In contrast, we develop an experimentally informed simulation using the parameters extracted from measurements: refractive index structure constant; mean flow rate; kinetic and thermal dissipation rates; Kolmogorov microscale; outer scale; and shape of the refractive index PSD. To confirm parameters measurements, the results are contrasted throughout the paper with previous studies, which found the same metrics for RB convection or underwater turbulence in water tanks [1,3,12,14,15,18,19,28,29].

A new tank has been constructed by the Naval Research Laboratory located in Washington, DC, and transferred to the United States Naval Academy, where experiments were performed. The tank, with dimensions $1.2\text{ m} \times 0.3\text{ m} \times 0.3\text{ m}$, is shown in Figs. 1(a)–1(c). In the RB tank, each plate contains the same stainless-steel immersion plate with the same heated and chilled water system structure, resulting in close-to-identical heating and chilling profiles. This allows us to assume the cold plate can take heat away from the system as uniformly as the hot plate brings it in. The RB tank has an aspect ratio (length/width) of one similar to previous studies; therefore, optical parameters are compared across prior studies with a similar tank aspect ratio, as shown in Table 1. For this work, the RB tank does not contain

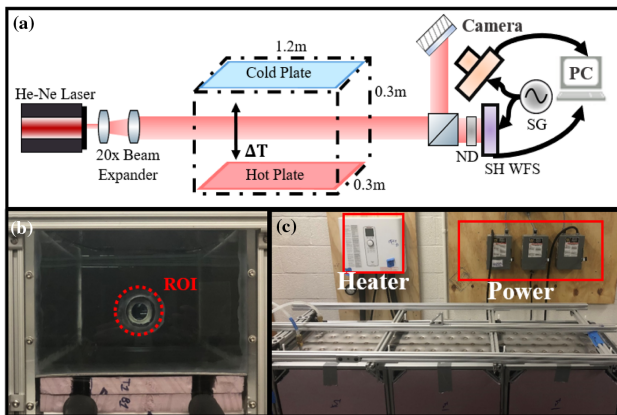


Fig. 1. (a) Experimental setup used to characterize the RB tank. Abbreviations are as follows: ND, neutral density filter; SHWFS, Shack–Hartmann wavefront sensor; SG, signal generator. (b) Image viewing through the RB tank where the laser beam propagates within the region of interest (ROI) in red. (c) Side view of the tank setup with water heater (left) and electrical power supplies.

Table 1. Summary of Published RB Turbulence Experiments and Their Parameters^a

Parameter	Tank 1 [1,12,14,15]	Tank 2 [18,19]	Tank 3 [28,29]
ΔT	2–10	3–5	10–25
L	0.5	0.6	0.1
$Ra \times 10^9$	5.0–25	13–22	0.2–0.7
$C_n^2 \times 10^{-10}$	0.1–10	0.66–1.4	9000–11000
l_0	2–3	—	1–2
L_0	28	10–20	4–33

^aNote the different impact of the characteristic length (L) and the temperature difference ($\Delta T^\circ\text{C}$) on Ra and $C_n^2[\text{m}^{-2/3}]$.

salt; thus, the focus can only be on the thermal fluctuations produced by the plates.

The first parameter of interest is the overall strength of the refractive index fluctuations, which can be quantified using the refractive index structure constant $C_n^2[\text{m}^{-2/3}]$. However, turbulence cannot just be quantified by its overall strength, as length scales over which energy dissipation occurs also characterize the turbulence. Energy dissipation occurs due to kinetic energy supplied by the largest eddy, quantified by the outer scale $L_0[\text{cm}]$, being dissipated to smaller eddies until viscosity is dominant. Since water's $Pr > 1$, the effects of momentum diffusivity could also affect energy dissipation, creating an inertial-convective region. As eddies break down further to small scales, thermal diffusivity becomes more effective, thus creating an inertial-diffuse region whose length scale is quantified by the inner scale $l_0[\text{mm}]$. The region between L_0 and l_0 is known as the inertial-subrange. These scales are listed in Table 1 for prior studies in three different RB tanks, along with the respective ranges of Rayleigh number.

From these length scales, other turbulence parameters can be derived such as the kinetic energy dissipation rate $\epsilon[\text{m}^2\text{s}^{-3}]$, thermal dissipation rate $\chi_T[\text{K}^2\text{s}^{-1}]$, Kolmogorov microscale η [mm], Batchelor scale $l_b[\text{mm}]$, mean flow velocity $U_m[\text{cm/s}]$, and Reynolds number. Each of these parameter's physical meaning and connection to previous studies will be discussed in later sections.

Using these experimentally measured parameters, a WOS simulation will be constructed with wavefront data using known refractive index PSDs, such as the Nikishov [30], Hill model-4 [10], and Von Kármán model [31], to verify the effectiveness of WOSs at capturing experimental trends. Verification of the WOS, employing the Hill model-4 spectrum, will be done with experimental data using temporally decorrelated statistical averages of the wavefront and intensity. Turbulence and optical parameters measured using the optical wavefront sensor will be discussed in Section 2 and similar results for optical intensity measurements in Section 3, followed by numerical simulations in Section 4 and the conclusion in Section 5. All technical methods, statistical observations, and mathematical definitions for the results are detailed in Appendices A–F.

2. WAVEFRONT CHARACTERIZATION

Wavefront statistics are obtained using a Shack–Hartmann wavefront sensor (SHWFS), which measures the local wavefront gradient that can be reconstructed into the beam's 2D phase profile accumulated during propagation. The 2D phase

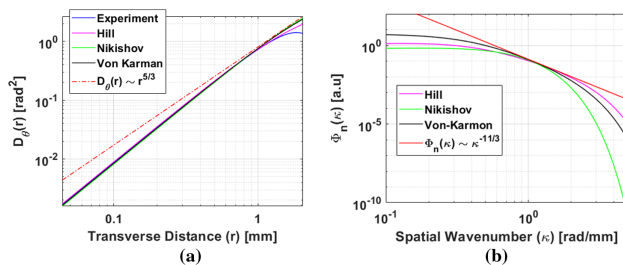


Fig. 2. Two different ways to represent the same phenomenological aspects of turbulence. (a) Experimental phase SF overlaid with fits to known refractive index PSD models with Kolmogorov 5/3 power law for reference. (b) Models of refractive index PSD fitted to phase SF data normalized to the Kolmogorov 11/3 power law slope for reference.

can then be decomposed into its Zernike mode decomposition representing a linear combination of optical aberrations induced by the turbulence. In Fig. 1(a), a Thorlabs WFS20 sensor, with a spatial resolution of 300 μm , is placed directly after the RB tank where a collimated 632.8 nm He–Ne laser is incident directly upon the detector. The SHWFS sensor output is set to obtain the first 55 Zernike polynomials (only the first 10 provide significant information) at 35 frames per second (FPS) with a 10 ms exposure time. The 2D phase profile is constructed in postprocessing with average wavefront tilt removed. The data set analyzed is 7000 samples of 2D phase realizations taken within a 3.3 min window to represent a more realistic averaging time of the turbulent effects. The temperature difference between the plates is set to 2°C and allowed 30 min to reach a steady-state before experiments are conducted. During the data collection the Rayleigh number is 1.1×10^9 , and the Prandtl number is 6.9. This ensures that wavefront perturbations remain weak to reduce SHWFS errors that could occur at a larger temperature difference.

The spatial statistics of the reconstructed wavefront are quantified by the phase structure function (SF), $D_\theta(r)$ [rad 2]:

$$D_\theta(r) = \langle [\theta(r + r') - \theta(r')]^2 \rangle, \quad (3)$$

where $r = (x^2 + y^2)^{1/2}$ is the separation distance between spatial coordinates, r' is the reference point within the 2D phase, and $\langle \dots \rangle$ is an ensemble average. The region of interest (ROI) of measurement is shown by the red beam outline in Fig. 1(b), which is illuminated by a beam with a 1.2 cm diameter and measurement limited by the SHWFS aperture diameter of 5.4 mm. The beam is centered at half the characteristic length to weaken wall effects on optical results.

The ensemble average of the phase SF is chosen over every twentieth image of the 7000 totals images to remove temporal-correlation between captures, leaving 350 realizations for analysis. Figure 2(a) shows the experimental $D_\theta(r)$ in blue centered at $r' = 0$. Statistical properties of homogeneity and isotropy are first tested.

A. Statistical Homogeneity and Anisotropy

To test the phase statistics for spatial homogeneity, the center of the phase SF is moved to about $r' = 0$ with details provided in Appendix A [32]. The points are only moved closely around the center since the ROI is where the most developed part of the

turbulence lies. A feature of the RB convection is turbulence intermittency, which can contribute to statistical homogeneity in space and time due to the RB model randomly producing convective thermal plumes leading to regions undergoing laminar-turbulent transition or well-mixed turbulence. These plumes are structured along the temperature gradient that creates a higher value of the phase SF in the direction of the temperature gradient [28,29]. For the 2° temperature difference presented in this work, the plumes do not significantly impact the temporal statistics compared with the spatial statistics. Over the course of the data collection, there is no observed time-structured dependency or periodicity suggesting that the turbulence generated by the RB convection is random and thus suitable for statistical studies using conventional models. It could also be from insignificant data averaging times where long-term averages of upward of 30 min may solve this issue [33].

Along with these observations, Appendix B shows evidence of anisotropy by viewing the structure function at varying azimuthal angles. The anisotropy is not significant enough to warrant full investigation at this moment; however, its effects will be included in the WOS model due to its presence in dictating intensity scintillation discussed further in Section 4.

B. Observation of Kolmogorov Statistics

The experimental data are observed to have a small inertial-subrange, which is evidence of underdeveloped energy dissipation or modest Reynolds number turbulence [34]. The power law of the phase SF within this region follows that of the Kolmogorov theory where, on average $D_\theta(r) \sim r^{5/3}$; therefore, assumptions of bounded Kolmogorov-type refractive index PSDs can be applied to the experimental data. In Appendix C, the data in this region are fit to non-Kolmogorov forms of the phase SF and show that the data in Fig. 2(a) do follow a Kolmogorov type inertial-subrange. This is illustrated by the portion of the experiment curve (blue) that follows the theoretical power law as the red dashed line.

This form of SF has also been observed in experimental temperature power spectra results bounded with a viscous-convective region [1,12]. Therefore, it will be assumed that Kolmogorov-type statistics can be assumed to fit the experimental phase SF; however, non-Kolmogorov properties have been reported in prior studies [15,28]. It is noted that isotropic, homogeneous, and Kolmogorov statistics are assumed in the remainder of this work, so that known models of optical turbulence can be applied for turbulent parameter estimation.

C. Measurement of Refractive Index Fluctuations

Random temperature fluctuations within a medium creates variations within the medium's refractive index, which affects light propagation. The strength of these variations can be quantified using the refractive index structure constant, $C_n^2[\text{m}^{-2/3}]$, which is a relevant parameter in any medium, including atmosphere and water [15,31]. In this experiment, only the water temperature varies the refractive index; therefore,

$$C_n^2 = \left(\frac{dn}{dT} \right)^2 C_T^2, \quad (4)$$

and the temperature structure constant is defined as

$$C_T^2 = 0.9\Gamma(1/3)\beta\chi_T\epsilon^{-1/3}, \quad (5)$$

where $\frac{dn}{dT}$ is the mean change of refractive index as a function of water temperature found to be $-1.08 \times 10^{-4} \text{ K}^{-1}$ at 632.8 nm [35], Γ is the gamma function, and $\beta = 0.72$ is the Obukhov–Corrsin constant [34]. The parameters χ_T and ϵ are general parameters of the turbulent flow that are connected to the fluid properties present, namely, the thermal diffusivity and kinematic viscosity, respectively [3,36–38]. Details of the estimation method using the phase SF are discussed in Appendix D with values reported in Table 2.

To quantify how much the turbulence impacts light propagation, two path averaged optical quantities are also introduced using the estimated values of C_n^2 [31]. The first being the Fried parameter (r_0 [mm]) of a plane wave that measures the coherence length of turbulence that is quantified using a Kolmogorov refractive index power spectrum (see Appendix E) defined as

$$r_0 = (0.423k^2 C_n^2 D_z)^{-5/3}, \quad (6)$$

where D_z is the propagation distance, $k = 2\pi n_0/\lambda$, λ is the optical wavelength, and $n_0 = 1.335$. The analytic form of the phase structure function in the inertial-subrange where a Kolmogorov refractive index power spectrum holds true is found to be [31]

$$D_\theta(r) = 6.88 \left(\frac{r}{r_0}\right)^{5/3}. \quad (7)$$

When a 5/3 slope is identified in the experimentally measured phase structure function, a point within this region, seen in Fig. 2(a), can be used to estimate the value of r_0 and then by Eq. (6) to obtain an estimate of C_n^2 .

The second metric is the Rytov number (σ_R^2 [-]) used as an estimate of the intensity variance defined for a plane wave propagating through turbulence following a Kolmogorov refractive index power spectrum as

$$\sigma_R^2 = 1.23 C_n^2 k^{7/6} D_z^{11/6}. \quad (8)$$

Results in Table 2 reflect the measured value of C_n^2 to be in reasonable agreement with path studies with similar Rayleigh numbers [14,15,18,19]. Large variations are noted due to the method of averaging chosen to remove temporal correlation, which induces turbulence intermittency needed for comparison, as shown in Section 4. Also, the optical turbulence strength is assumed to be isotropic along the length of the tank due to uniform heating; however, wall effects at the tank ends, thermal plumes, or nonuniform plate heating could skew data or induce variations.

Table 2. Estimated Optical Turbulence Strength Parameters of Refractive Index Structure Constant C_n^2 , Fried Parameter r_0 , and Rytov Number σ_R^2 , Using the Plane Wave Phase SF Calculated from Methods in Appendix D along the X and Y Directions

Axis	r_0 [mm]	σ_R^2	C_n^2 [m $^{-2/3}$]
X	3.89 ± 1.51	0.050 ± 0.070	$2.56 \pm 1.55 \times 10^{-10}$
Y	3.71 ± 1.47	0.052 ± 0.065	$2.76 \pm 1.67 \times 10^{-10}$

The values of r_0 reflect “strong” turbulence compared with atmospheric statistics whose r_0 typically falls within m–cm scales with a longer path length to accumulate turbulent perturbations. In air, the Prandtl number is on order unity, resulting in different turbulent fluctuations than those of water [10,11]. Although r_0 is small and C_n^2 is large, the Rytov number remains in the region of weak intensity scintillation [31].

D. Fitting to Known Refractive Index PSDs

Leveraging the assumption that Kolmogorov statistics can be applied in the observed inertial-subrange, many theoretical refractive index PSDs ($\Phi_n(\kappa)$) can be applied to fit the observed phase SF. The refractive index PSD is directly proportional to the phase PSD ($\Phi_\theta(\kappa)$) by the relationship [39]

$$\Phi_\theta(\kappa) = 2\pi k^2 D_z \Phi_n(\kappa), \quad (9)$$

where $\kappa = (\kappa_x^2 + \kappa_y^2)^{1/2}$ is the radial spatial wavenumber. Due to the collimated nature of the Gaussian beam used, the form of a plane wave phase SF is assumed, defined as [31]

$$D_\theta(r) = 8\pi^2 k^2 L \int_0^\infty \kappa \Phi_n(\kappa) [1 - J_0(\kappa r)] d\kappa, \quad (10)$$

where J_0 is a zeroth-order Bessel function. Inverting Eq. (10) can prove difficult using the formal relationship between $\Phi_n(\kappa)$ and $D_\theta(r)$ [31]. Instead, spectral fits are done using a nonlinear Levenberg–Marquardt method to Eq. (10) using known models of the refractive index PSD. The spectra analyzed, shown in Appendix E, are the Nikishov–Nikishov model for turbulent water with salinity dependence removed [30], Hill model-4 bounded with a Tatarskii outer-scale cutoff instead of an exponential [10], and the von Kármán spectrum [31].

The main difference between each model are length-scale cutoff functions between the outer scale and inertial-subrange or inertial-subrange and viscous-diffuse region. Table 3 shows the calculated model parameters for each refractive index PSD model fit to experimental data. The first length scale being Kolmogorov microscale (η), which are the smallest structures in the turbulent field due to dissipation of kinetic energy; however, once initial mixing stops, diffusion occurs to homogenize the medium where these small-scales are quantified using the Batchelor scale (l_b) [10]

$$l_b = (\nu D_T^2 / \epsilon)^{1/4}. \quad (11)$$

The inner scale, l_0 , can be related to η using [34]

$$l_0 = [(28/5)\beta\Gamma(1/3)Pr]^{3/4}\eta. \quad (12)$$

Table 3. Parameters Obtained from Matching Experimental Phase SF Data to the Power Spectra of Interest

Spectrum	η [mm]	l_b [mm]	l_0 [mm]	L_0 [cm]
Nikishov	0.5	0.2	0.7	6.1
Hill model-4	0.6	0.2	0.8	1.73
von Kármán	2.2	0.5	3.3	1.50

The resulting phase SF for each model is shown in Fig. 2(a), alongside the experimental data with the shape of the fit refractive index PSD in Fig. 2(b). A red line illustrates the inertial-subrange power law $\Phi_n(\kappa) \sim \kappa^{-11/3}$.

By inspection, the different small- and large-scale cutoff functions result in a varying lengths of the inertial-subrange. These length values of millimeter scale agree with those reported in the literature [12]. From this fitting procedure, the Hill model-4 is deemed the best fit for the data. It contains the most reasonable values of the length scales presented in Table 3 compared with calculations in Appendix E and Table 3. Furthermore, the Hill model-4 contains a rigours physical derivation and inclusion of a viscous-convective region, which occur in water [10,38,40]. With this model of the refractive index PSD formulated, a numerical WOS can now be constructed to compare with the experimental results.

Outer scale estimation is presented in Appendix F to be 4 cm and agrees with the order of magnitude obtained from fits to the refractive index spectrum for each functional shape reported in Table 3. However, when compared with other experiments, the theoretical and experimentally calculated value do not agree with the typical assumption of the outer scale being the width or half the width of the RB tank. It is interesting that measured values, for an RB tank with a width of 60 cm, of outer scale were seen to be 10–20 cm [18]. The same occurred for an RB tank with a width of 50 cm where outer scales of 28 cm were reported [14].

3. INTENSITY CHARACTERIZATION

The second part of this experimental data is the synchronization of the intensity images from the camera shown in Fig. 1(a). The camera is a Fastec TS5 sampling at 70 FPS, triggered using the signal generator with the 35 Hz sync signal, where the first frame of each trigger is used for comparison. Data are taken during the same 3.3 min duration as the SHWFS. Each frame has 500×500 pixels with $60 \mu\text{m}$ pixel resolution, 12-bit intensity resolution, and average of 10 image captures to reduce pixel noise. An image of an experimental realization is shown in Fig. 4(a), which exhibits thread-shaped intensity profiles.

An intensity image is selected from every twentieth realization to keep in-sync with the wavefront measurements while removing correlations among the intensity images to calculate scintillation in Fig. 4(c). The 2D scintillation in Fig. 4(c) is calculated using [31]

$$\sigma_I^2(x, y) = \frac{\langle I^2(x, y) \rangle - \langle I(x, y) \rangle^2}{\langle I(x, y) \rangle^2}. \quad (13)$$

A circle mask is placed across the scintillation profile that is four times the beam waist of 6 mm to reduce camera-induced noise around the edge of the beam. The experimental scintillation contains various spatial structures rather than an isotropic-sized speckle. The on-axis scintillation, selected from 30 centered points, is 0.04 ± 0.005 , whereas the total average scintillation is 0.09 ± 0.003 with uncertainty calculated from the respective standard deviations of the data points. These values are roughly in agreement with the theoretical Rytov number calculated in

Table 2; however, the uncertainty in the Rytov number is related to the large uncertainty within the measured C_n^2 .

A. Estimation of Energy Dissipation via Intensity

Due to the sampling rate of the camera capturing correlated realizations of the intensity, a mean flow rate can be estimated. The mean flow velocity U_m is measured by applying circular masks in postprocessing, where the time varying intensity fluctuations within each mask can be cross-correlated. The temporal shift of the correlation peak divided by the synthetic aperture distance results in the mean flow [41]. Mean flow, U_m , was estimated to be 1.5 ± 0.4 cm/s corresponding to Reynolds number of 4.6×10^3 within the ROI. Previous RB tank studies reported values of U_m to be up to 2 cm/s in similar Ra conditions using an acoustic doppler velocimeter [12]. Similar magnitude flows of 8 cm/s in the vertical and 4 cm/s in the horizontal were measured in the same tank used in [12] using an LED board array [14].

Using U_m and the value of C_n^2 , the kinetic and thermal dissipation rates can be calculated. The kinetic dissipation rate ϵ is found from the temperature structure constant ($C_T^2 [\text{K}^2 \text{m}^{-2/3}]$), which is related to C_n^2 by Eq. (5). The estimated values of the average dissipation rates and length scales using three methods of calculation are displayed in Table 4. Method 1 uses the relationship between η , found from being fit to Hill model-4 in Table 3, and ϵ using

$$\eta = (v^3/\epsilon)^{1/4}, \quad (14)$$

and Eqs. (4) and (5) with the value of C_n^2 in Table 2 to find χ_T .

The second method finds χ_T , independent of C_n^2 , using observational statistics of Rayleigh number (Ra) and Reynolds number (Re) from computational fluid dynamic simulations (CFD) of RB convection at high Ra [42] and leveraging GL theory [27]. The measured value of U_m can be used to calculate the Re within the center of the tank that is related to the Ra using $\text{Ra} \sim \text{Re}^{2.22}$ observed from CFD [42].

The beam illuminates a volume of convection that effectively makes a measurement of the mean volume averaged $\langle \chi_V \rangle$. Using GL, the total dissipation is the sum of plume and bulk background mean dissipation rates as [27,42]

$$\langle \chi_V \rangle = \frac{V_{pl}}{V} \langle \chi_{pl} \rangle + \frac{V_{bg}}{V} \langle \chi_{bg} \rangle, \quad (15)$$

where V is total volume of the measurement, V_{pl} is the thermal plume volume, V_{bg} is the background bulk volume, $\langle \chi_{pl} \rangle$ is

Table 4. Estimated Dissipation Rates and Turbulent Length Scales Using Three Different Methods^a

Quantity	Method 1	Method 2	Method 3
$\epsilon \times 10^{-6} [\text{m}^2 \text{s}^{-3}]$	7.79	0.43	0.11
$\chi_T \times 10^{-4} [\text{K}^2 \text{s}^{-1}]$	2.46	0.94	0.59
$l_0 [\text{mm}]$	0.8	2.4	1.7
$l_b [\text{mm}]$	0.2	0.1	0.1
$\eta [\text{mm}]$	0.6	0.5	0.5

^aMethod 1 uses the Kolmogorov microscale fit from Hill model-4 to calculate dissipation rates using Eq. (14). Method 2 calculates dissipation rates using Eq. (16) from CFD models using the experimentally measured value of the Reynolds number from mean flow. Method 3 calculates dissipation with Eq. (16) using the calculated Rayleigh number in Section 2 ($\text{Ra} = 1.1 \times 10^9$).

the thermal plume dissipation, and $\langle \chi_{bg} \rangle$ is the thermal bulk dissipation. From CFD, it is shown that $\langle \chi_V \rangle \text{Ra}^\gamma$ for plume and background regions [42]. If averaging volume contains a 0.1% volume fraction, for a tank with an aspect ratio of 1, the thermal dissipation is observed as

$$\langle \chi_V \rangle = \frac{\Delta T^2 U_f}{L} (0.15 \text{Ra}^{-0.22} + 0.32 \text{Ra}^{-0.22}), \quad (16)$$

where $\text{Ra} = \text{Re}^{2.22}$, $U_f = \sqrt{g D_T \Delta T L}$ is the free-fall velocity, and $\text{Re} = U_f L / v$ is the Reynolds number [25].

The third method does not use the measured Ra from the Re number; instead, it uses the precalculated $\text{Ra} = 1.1 \times 10^9$ to find χ_T . Table 4 summarizes the calculated dissipation rates from each estimation method. Due to the smallest length scales varying with estimation of ϵ following from Eqs. (4) and (5), l_0 , l_b , and η are also shown in Table 4.

Matt *et al.*'s [12] data taken from an acoustic doppler velocimeter measured the cross sectional kinetic and thermal dissipation rates within the inertial-subrange on the orders 10^{-7} and $10^{-3} - 10^{-4}$ similar to Table 4 for $\text{Ra} \sim 10^{10}$. Comparison of the dissipation rates in Table 4 show lower values; however, this is for a Ra number with a one order lower magnitude. Therefore, estimates in Table 4 would be expected to be less than previous reports, making them a reasonable estimate without direct measurement of the immediate temperature or velocity field.

The length scales also fall within a reasonable value. Batchelor scale estimates in this tank fall within the expected values of water, where calm water can be on the order of 2 mm, whereas the most turbulent can be as small as 0.2 mm [3].

4. CONSTRUCTION OF WAVE-OPTICS SIMULATION

WOSs can be developed using experimentally informed parameters leveraging the turbulent measurements found through synchronous wavefront and intensity measurements in Sections 2 and 3. The values of C_n^2 , ϵ , χ_T , η , $d\eta/dT$, and $\Phi_n(\kappa)$ following Hill's model-4 are chosen in the WOS to better represent the experimental findings. The goal of this section is to compare the subtleties between WOS simulations and real data. WOSs place significant assumptions on the turbulence present; therefore, this comparison is done to better the experimental features captured by simulations. Both intensity and phase statistics can be compared with experimental results by leveraging the synchronous intensity and wavefront measurements.

WOS simulations model the coherent effects of random phase noise on a laser wavefront [43]. The phase noise is implemented as a phase-only distortion whose phase PSD is sampled from the Hill model-4 refractive index PSD. The spatial distribution of phase shifts is found using [44]

$$\theta(x, y) = \int_{-\infty}^{\infty} \int_{-\infty}^{\infty} (a + ib)[\Phi_\theta(\kappa)]^{1/2} e^{i(\kappa_x x + \kappa_y y)} d^2\kappa, \quad (17)$$

where a and b are normal distributed random numbers. Beam propagation is done using a modification of the code in previous works, where a subharmonic sampling of the refractive index

Table 5. Simulation Parameters Used for All Simulations Presented in This Paper

Parameter	Notation	Value
Grid size [cm]		2.5 × 2.5
Grid sample	N_g	2048 × 2048
Grid spacing [μm]	δ	12.2
Propagation distance [m]	D_z	1.2
Propagation steps	N_z	1.2
Propagation spacing [m]	Δz	0.25
Wavelength [nm]	λ	632.8
Initial spot size [mm]	w_0	6
Kolmogorov microscale [mm]	η	0.6 ± 0.65
Outer scale [cm]	L_0	1.73 ± 4.5
Anisotropy	μ_a	0.8 ± 0.55
Refractive index [$\text{m}^{-2/3}$]	C_n^2	2.5 ± 1.5 × 10 ⁻¹⁰

PSD is implemented [45]. The numerical grid parameters of the simulation are listed in Table 5.

One modification to the WOS is that the following parameters become Gaussian random variables with mean and standard deviation that are empirically determined, as listed in Table 1: Kolmogorov microscale; outer scale; anisotropy; and refractive index structure parameter. This is done due to the significant variation within the frame-to-frame wavefront and intensity exhibiting changing length scales. This is especially prevalent within the intensity and scintillation results discussed in the next section.

Assuming the propagation distance is uniformly heated creating a constant C_n^2 across the path leading, the simulation uses four uncorrelated phase screens placed at equidistant lengths along the path of 1.2 m.

A. Wavefront and Intensity Comparison

The first metric to compare between simulation and experiment is the reconstruction of the expected form of the phase SF. Figure 3 shows the experimental, theoretical calculated phase SF using Eq. (3), and simulated phase SF using a WOS in the x and y directions. The resulting phase SF, shown in green in Fig. 3, provides a good fit to the experimental results. This results in the WOS being able to average independent realizations, containing turbulence using uncorrelated realizations, can be recreated

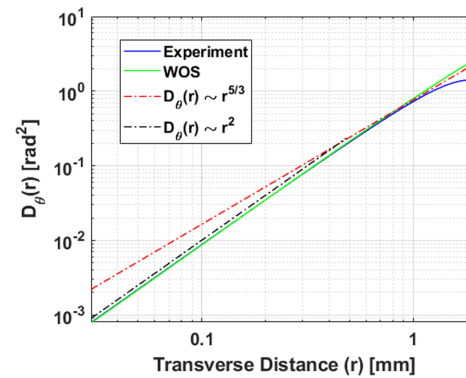


Fig. 3. Comparison of experimental phase SF with a simulated phase SF using the informed WOS model. Dashed red line is the Kolmogorov 5/3 slope of the phase SF; the dashed purple is the slope of a parabolic structure function.

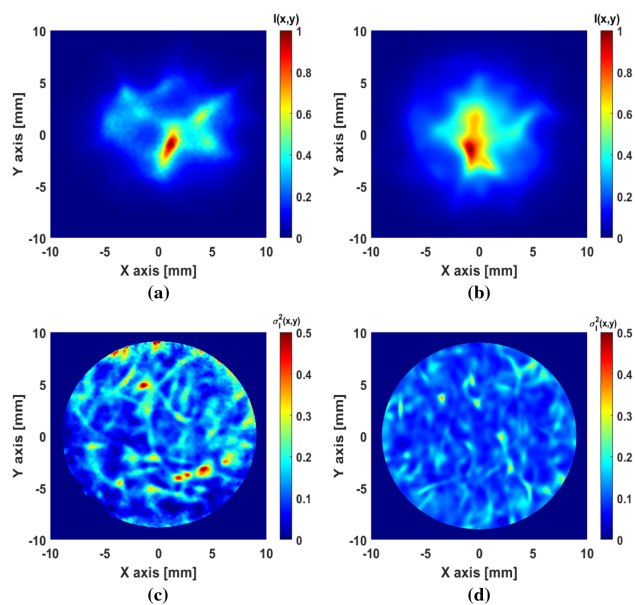


Fig. 4. (a) Experimental intensity realization. (b) Simulation of (a). (c) Experimental scintillation over 350 intensity realizations. (d) Simulation of (c).

within the simulation and on average will converge to the proper SF given l_0 , L_0 , μ_a , and C_n^2 are varying between each realization.

To provide further comparison of the recreated phase statistics, the intensity or fourth-order statistics can also be compared. The simulated intensity profile in Fig. 4(c) captures the subtle thread-like structure and smaller scale “holes” of low intensity as the experimental data. However, a significant feature of the RB turbulence captured in the simulations is the scintillation in Fig. 4(d), which contains various streaks due to the addition of varying the η , L_0 , and μ_a . The simulated scintillation within an aperture four times the beam waist, similar to Section 3, is 0.054 ± 0.0003 , whereas the on-axis scintillation is 0.048 ± 0.0003 , which is closer to the experimental value. If these were not given their own individual mean and variance, the spatial scintillation statistics would not resemble the experimental data.

To further quantify the similarities between the intensity and scintillation, ensemble averaged statistics are as calculated in Fig. 5. The first is the correlation function of the 2D scintillation index, described in Eq. (13), in Fig. 5(a). The correlation function shows the average feature correlation length along X and Y slices through the 2D scintillation. To reduce the effects of individual realizations, the scintillation PSD is calculated in Fig. 5(b) using the Wiener–Khinchin theorem. The simulated and experimental data along the X and Y directions follow a similar slope and amplitude. This shows that the simulation, based on experimental phase measurements, is able to capture the size and amplitude of the scintillation features seen in RB convective turbulence.

A similar analysis is done for the intensity features, where the ensemble averaged PSD is as calculated and displayed in Fig. 5(c). The intensity PSD contains low and high spatial frequency features where a small peak occurs at low κ . As κ increases, the slope begins to decay the same in the X and Y directions in the experimental and simulated data. However,

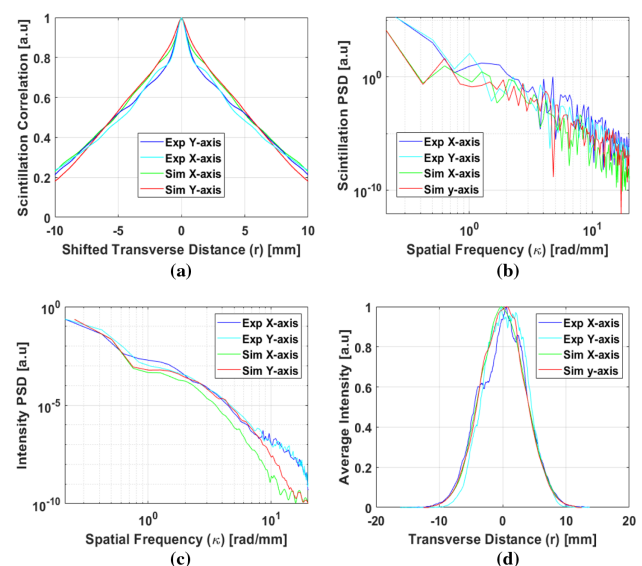


Fig. 5. Demonstration of agreement between experimental and simulated intensity statistics. (a) Autocorrelation cross section of the 2D scintillation profile of the experimental [Fig. 4(c)] and simulated [Fig. 4(d)] data in the X and Y directions. (b) Scintillation PSD cross section calculated from (a). (c) Average intensity PSD cross section of the experimental and simulated data across 350 realizations. (d) Average intensity cross section of the experimental and simulated data across 350 realizations.

at high spatial frequencies, before the camera noise floor, there are components of the experimental intensity variance that the simulations do not capture. These frequencies correspond to length scales of roughly 0.6 mm corresponding to the smallest length scales of the turbulence. The simulations are able to capture this feature for most of the experimental intensity PSD until high-frequency camera noise begins to dominate, which is then cut off by the axis limits in Fig. 5(c). In Fig. 5(d), the average intensity profile along the X and Y directions are compared and indicate no significant beam breakup through the turbulence and similar average shapes that maintain the original Gaussian nature of the beam. The experimental data contains high-frequency camera noise after a low-pass filter is applied to each image realization.

5. CONCLUSIONS

Within this study, characteristics of RB convection were estimated by a synchronous optical wavefront and intensity measurements. The experimental data were analyzed to show that the wavefront statistics were inhomogeneous, anisotropic, and with strong to moderate levels of turbulence strength and length scales exhibiting a small Kolmogorov inertial-subrange at millimeter-length scales. Experimentally informed numerical wave optic models using the Hill model-4 for random phase generation are seen to be in good agreement with experiment data. Results were compared with those in previous experiments in RB tanks, where C_n^2 values were comparable with other reports for similar Ra numbers, whereas the length-scale estimates of $L_0 \sim 1.5$ cm and $l_0 \sim 0.8$ mm were different, lending to effects of the measurement apparatus dictating how well scale sizes are resolved, especially outer scales. The turbulence in this

tank exhibits Batchelor scales on the order of 0.2 mm and C_n^2 values consistent with oceanic turbulence, lending this RB tank a good testing platform for undersea optical applications [15].

The numerical wave optics model based on random phase screens created from the experimental wavefront statistics was compared with experimental data. By comparing the simulations directly to experiments, it also highlighted the need for multiple phase screen parameters to become random variables, which could capture more subtle effects on laser beam propagation. These parameters include anisotropy, C_n^2 , inner scale, and outer scale. Depending on the assumptions of the simulation, power law of the refractive index PSD can also be varied.

This work leads to the need of further experimentation of the RB tank at different temperature differences to understand the effects of laser propagation in varying Ra numbers. By varying the Ra number, the selected simulation parameters and refractive index must be revisited, as the turbulence may change statistics significantly if a different inertial-subrange or viscous-convective range appear within the wavefront statistics. Since this data displayed a small inertial-subrange, the values of Ra number must be larger to exhibit more developed turbulence. Future work will entail quantifying the temporal statistics of the turbulence and propagation of various forms of spatially structured light.

APPENDIX A: OBSERVATION OF STATISTICAL HOMOGENEITY

Statistical homogeneity of the phase SF is calculated by moving the reference point r' within the numerical grid, as shown in Fig. 6. Figure 6 also shows the 2D SF centered at point L1 $r' = 0$ and other points at a distance of 0.15 mm centered around this point, shown as the different shapes overlaid on 6. Each point (L#) is labeled with a color and respective marker, which correspond to the phase SF calculated in Fig. 6(b). The SF is calculated from the same set of 350 phase realizations discussed in Section 2. By inspection of Fig. 6(a), the features contained in the SF are not homogeneous around the azimuth, so when the center is shifted, these features create inhomogeneities. This asymmetry leads to the turbulence not being homogeneous across the detector aperture for small transverse separations; however, larger distances that correspond to the inertial-subrange appear a bit more homogeneous as the slopes of the SF converge slightly in Fig. 6(b). If the different centered

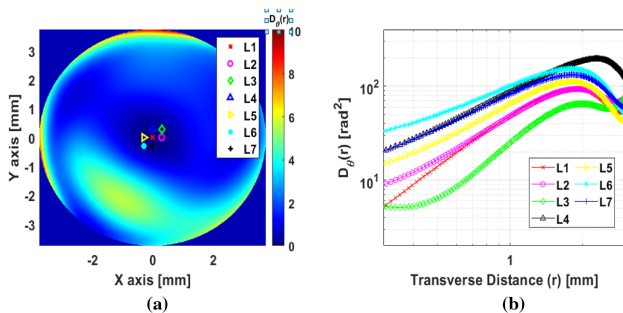


Fig. 6. Determination of statistical homogeneity. (a) Heatmap of the averaged experimental 2D phase SF located at $r' = 0$ overlaid by location of varying observation points. (b) Cross section for given observation points.

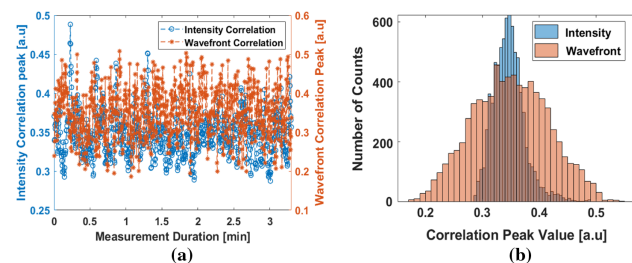


Fig. 7. Determination of turbulence intermittency. (a) Correlation peak value of the intensity and wavefront time series for the 3 min data duration. (b) Histogram of the correlation peak fluctuations for the intensity and wavefront time series.

phase SFs in Fig. 6(b) overlaid, then the turbulence would be considered homogeneous.

The spatial inhomogeneities within the phase SF can be considered due to the presence of plume structures that are randomly generated due to the RB convection. Another concern is the temporal intermittency that generates the random plumes. The process of mixing in a turbulent flow is inherently a random process leading to internal intermittency, where thermal plumes rise and fall within the tank, where at specific instances of time the fluid may be well mixed or laminar [46]. As the flow is not driven by a mechanical force, there are no effects of external intermittency. To quantify that the turbulence during the measurement duration is not significantly intermittent, a temporal correlation peak can be used to show that, during the duration of the measurement, the fluctuations are random and not significantly structured, as would be expected if the turbulence is significantly intermittent. Figure 7(a) shows the correlation peak as a function of measurement duration for the intensity and wavefront data. The correlation is taken between two frames to determine if things are changing significantly faster than they were sampled. Large jumps within the correlation peak to either high correlation (value of 1) or low correlation (value of 0) are an indication of intermittency. From inspection of both plots in Fig. 7(a), there is no significant change in correlation. The correlation peak varies are randomly illustrated in Fig. 7(b) where histograms of the correlation peak for intensity and wavefront data are plotted. The deviation of the wavefront is larger, as it is more sensitive to changes of the refractive index.

APPENDIX B: OBSERVATION OF ANISOTROPIC TURBULENCE

To confirm the presence of anisotropic effects, the 2D phase SF is analyzed at different angles along the azimuth, as illustrated in Fig. 8(a). Five angles are calculated, i.e., 0°, 30°, 45°, 60°, and 90°, as shown in Fig. 8(b). The dotted and solid lines correspond to the same respective angle of the slice in Figs. 8(a) and 8(b).

Each axis contains a similar shape of the SF that has an outer-scale drop-off at high spatial separations determined due to the SHWFS aperture (limited by the Gaussian beam width), a small inertial-subrange, and a tail that extends to low separation distances. Each SF chosen along the third quadrant angles shows a larger value and slightly different shape of the phase SF. This leads to the observation that anisotropic effects must be taken into account when modeling the phase realizations.

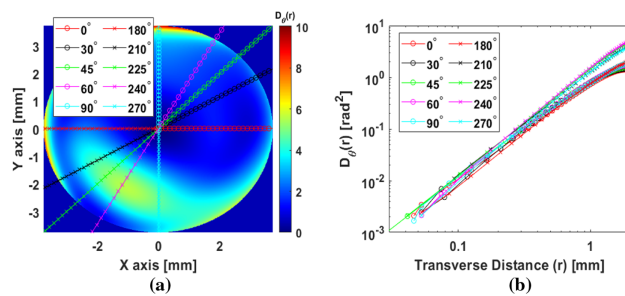


Fig. 8. Observation of statistical anisotropy. (a) Same as Fig. 6(a) with overlaid axis of observation. (b) Cross section along given observation axis.

The differences between the inherent shapes of the SFs may also indicate a change in length scales present between realizations or change in power law along different directions due to the change in slope along the y axis, which could be a change in power law along the thermal gradient.

APPENDIX C: ESTIMATION OF INERTIAL-SUBRANGE POWER LAW

To understand if the observed phase fluctuations contain a Kolmogorov inertial-subrange, the predicted 5/3 of the phase SF, corresponding to a 11/3 refractive index power law, is fit to a general non-Kolmogorov phase SF. The general form of a power law 2D phase SF is [47]

$$D_\theta^{nk}(r) = c_1(\alpha) \left(\frac{r}{\hat{r}_0} \right)^{\alpha-2} \quad (\text{C1})$$

with a generalized phase power spectrum

$$\Phi_\theta(\kappa) = (2\pi)^2 B(\alpha) c_1(\alpha) \hat{r}_0^{2-\alpha} \kappa^{-\alpha} \quad (\text{C2})$$

with

$$B(\alpha) = \frac{\Gamma(\alpha/2)}{2^{2-\alpha} \pi \alpha \Gamma(-\alpha/2)}, \quad c_1(\alpha) = 2 \left(\frac{8}{\alpha-2} \Gamma \left[\frac{2}{\alpha-2} \right] \right), \quad (\text{C3})$$

where α is the power law of the phase power spectrum, and \hat{r}_0 is the effective non-Kolmogorov Fried parameter. This fit ignores any inner and outer scale effects, as only the linear portion of the inertial-subrange is of concern. A ratio of the data points selected in Fig. 9(a) and Eq. (C1) with varying values of α called $D_\theta^{nk}(r)/D_\theta^{\exp}(r)$. The ratio $D_\theta^{nk}(r)/D_\theta^{\exp}(r)$ is taken and then fit to a line using a linear least-squares method. A plot of the fitted line's slope as a function of α is plotted in Fig. 9(b), where the zero crossing represents the non-Kolmogorov power law of best fit to the experimental data.

It is observed that the best fit [green line in Fig. 9(b)] does occur around a phase SF power law of 5/3 corresponding to a Kolmogorov inertial-subrange [red line in Fig. 9(b)]. Therefore, even at a relatively small Ra number indicative of “weaker” turbulence, a region of 1 mm spatial separation containing a Kolmogorov power law inertial-subrange is observed in this data set. For fitting purposes in Section 2.D, $\alpha = 11/3$ to keep parameters limited to the familiar definitions of C_n^2 , l_0 , and L_0 since these will change for non-Kolmogorov α [28].

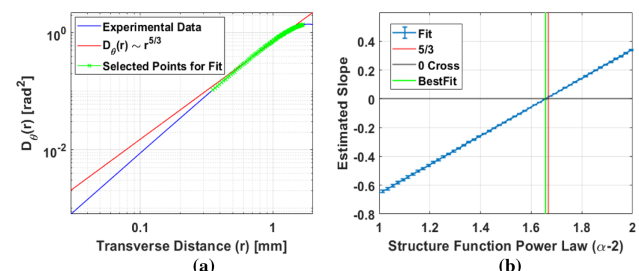


Fig. 9. Estimation of the inertial-subrange power law. (a) Comparison of experimental data and Kolmogorov SF 5/3 power law with selection of inertial-subrange. (b) Estimated slope of the structure function ratio $D_\theta^{nk}(r)/D_\theta^{\exp}(r)$ corresponding to $\alpha - 2 = 1.65$.

APPENDIX D: FLUCTUATIONS OF EFFECTIVE C_n^2 ESTIMATE

Estimation of C_n^2 is done using the analytic form of the phase SF that is found within the inertial-subrange by Eq. (4) with the definition of the Fried parameter from 6 at a particular value of r . Using different forms of the analytic phase SF, it can be seen that C_n^2 will change depending on the other effective parameters in the desired model. If a point is chosen outside the inertial-subrange, then more complex phase SF models must be calculated in closed form. In Fig. 10(a), the black vertical and horizontal lines correspond to a point that can be used to estimate C_n^2 . By taking the value of $D_\theta(r)$ and r , the Fried parameter, whose fluctuations depend on the variance within the phase SF data, can be estimated.

To further understand the fluctuations, the C_n^2 fluctuations within the data set are displayed as a probability distribution in Fig. 10(b) fitted to a Weibull distribution of the form

$$f(\rho, k, \lambda) = \frac{k}{\lambda} \left(\frac{\rho}{\lambda} \right)^{k-1} e^{-(\rho/\lambda)^k} \quad (\text{D1})$$

with $k = -10.2$ and $\lambda = -14$. This distribution follows any variable dependent explicitly on C_n^2 . The distribution nature signifies that a weaker turbulence effect is more likely to be observed, which could be due to thermal plumes. A distribution of this nature is able to represent the skewness in the data as compared with more traditional Gamma–Gamma or lognormal methods [31].

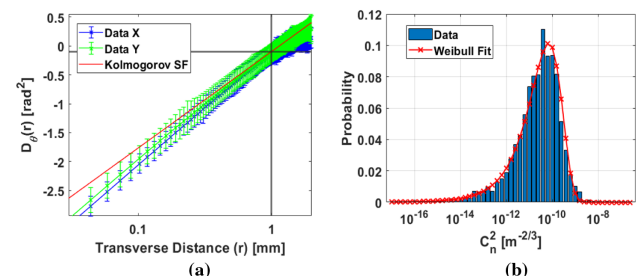


Fig. 10. Average experimental phase SF in the X and Y directions calculated using Eq. (3) with Kolmogorov power law for reference in red. (a) Crosshair shows a sample data point used to calculate Fried parameter. (b) Experimental data histogram of $\log_{10}(C_n^2)$ fit to a Weibull distribution.

APPENDIX E: INDEX OF FITTED REFRACTIVE INDEX PSDs

A list of the fitted refractive index PSDs and their input parameters is provided. The refractive index is proportional to the temperature using $n(x, y) = -\alpha T(x, y)$, where α is taken to be $\times 10^{-4}$ liter/deg [30].

A. Nikishov–Nikishov

The Nikishov–Nikishov spectrum, originally developed for the inclusion of salinity and temperature effects, is modified here to remove salinity and include a Tatarskii outer-scale cutoff [39]

$$\Phi_n(\kappa) = 0.388 \times 10^{-8} C_n^2 [\kappa^2 + \kappa_0^2]^{-11/6} [1 + 2.35(\kappa\eta)^{2/3}] f(\kappa, w), \quad (\text{E1})$$

where $C_n^2 = \epsilon^{-1/3} \chi_T$ and $\kappa_0 = 2\pi/L_0$. $f(\kappa, w)$ is a function of the ratio of temperature to salinity contribution defined as

$$f(\kappa, w) = \frac{1}{w^2} (w^2 e^{-A_T \delta} + e^{-A_S \delta} - 2w e^{-A_{TS} \delta}), \quad (\text{E2})$$

where $A_T = 1.863 \times 10^{-2}$, $A_S = 1.9 \times 10^{-4}$, $A_{TS} = 9.41 \times 10^{-3}$, and $\delta = 8.284(\kappa\eta)^{4/3} + 12.978(\kappa\eta)^2$. In this work, $w = -5$ to remove effects of salinity.

B. Hill Model-4

Hill fit four scalar spectral transfer models to experimental data and found that each have the Kolmogorov ($\kappa^{-5/3}$) inertial-subrange and a viscous-convection range following a Batchelor spectrum (κ^{-1}) leading into the viscous-diffuse region [10]. This model includes an exponential cutoff in comparison with the Von Kármán spectrum [40]. The spectrum is modified here to contain a Tatarskii type outer scale cutoff:

$$\Phi_T(\kappa) = \frac{\beta \epsilon^{-1/3} \chi_T}{4\pi} [\kappa^2 + \kappa_0^2]^{-11/6} g_t(\kappa\eta), \quad (\text{E3})$$

where $\beta = 0.72$ is the Obukhov–Corrsin constant, the nondimensional function

$$g_t(x) = \sum_{j=0}^2 a_j x^{b_j} e^{-174.90x^2 c_t^{0.96}}, \quad (\text{E4})$$

where $\{a_j\} = \{1, 21.62c_t^{0.02}, -18.18c_t^{0.04}\}$, $\{b_j\} = \{0, 0.61, 0.55\}$, $c_t = a^{4/3} \beta Pr_T^{-1}$, Pr is the temperature Prandtl number, and $a = 0.072$ is a constant. It is assumed that the power law will not vary to fit the observed Kolmogorov $5/3$ power law within the phase SF data. Equation (E3) is for the temperature fluctuations, which can be converted to the refractive index spectrum following

$$\Phi_n(\kappa_a) = \left(\frac{dn}{dT} \right)^2 \mu_a^2 \Phi_T(\kappa_a), \quad (\text{E5})$$

where $\frac{dn}{dT}$ is the same as Eq. (4), $\kappa_a = [\kappa_x^2 + (\mu_a \kappa_y)^2]^{1/2}$, and μ_a determines the amount of anisotropy present in the spectrum [48].

C. Von Kármán Spectrum

The von Kármán spectrum contains analytically tractable inner- and outer-scale cutoff functions; however, they do not lend the same physical derivations as the previous two models. The refractive index PSD is defined as [31]

$$\Phi_n(\kappa) = 0.033 C_n^2 \exp[-(\kappa/\kappa_m)^2] (\kappa^2 + \kappa_0^2)^{-11/6}, \quad (\text{E6})$$

where $\kappa_m = 5.92/l_0$.

D. Kolmogorov Spectrum

The Kolmogorov spectrum contains no inner- or outer-length scale cutoff, which leads to analytic results; however, the physical conditions may not always produce statistics that follow this spectrum. The spectrum can be used to estimate parameters when an inertial-subrange following Kolmogorov statistics is present in the data without reformulation of the refractive index power spectrum. The refractive index PSD is defined as [31]

$$\Phi_n(\kappa) = 0.033 C_n^2 \kappa^{-11/3}. \quad (\text{E7})$$

APPENDIX F: ESTIMATION OF OUTER SCALE

Outer-scale measurements can be made from temporal data using Taylor's frozen approximation; however, Tatarskii derived an estimate for the outer scale with the inclusion of buoyancy forces being related to C_T^2 [49]:

$$C_T^2 = \frac{0.9 \Gamma(1/3) \beta}{Pr} \frac{\Delta T}{L} L_0^{4/3}, \quad (\text{F1})$$

which has been used before for atmospheric outer scale measurements [50]. Using Eq. (4) with the estimate of C_n^2 in Table 2, the outer scale is calculated to be 4 cm, which is on order of magnitude as estimated by fitting the phase SF using the Hill model-4 spectrum of 1.7 cm. The measurement of outer scale may be limited by the beam diameter or aperture of the SHWFS.

Funding. U.S. Department of Defense (SMART SEED Grant).

Acknowledgment. Thank you to the reviewers for their time and excellent comments, which improved this paper.

Disclosures. The authors declare no conflicts of interest.

Data availability. Data underlying the results presented in this paper are available upon request.

REFERENCES

1. W. Hou and S. Matt, "EO signal propagation in a simulated underwater turbulence environment," in *OCEANS - TAIPEI* (2014), pp. 1–6.
2. Y. Ren, L. Li, Z. Wang, S. M. Kamali, E. Arbabi, A. Arbabi, Z. Zhao, G. Xie, Y. Cao, N. Ahmed, Y. Yan, C. Liu, A. J. Willner, S. Ashrafi, M. Tur, A. Faraon, and A. E. Willner, "Orbital angular momentum-based space division multiplexing for high-capacity underwater optical communications," *Sci. Rep.* **6**, 33306 (2016).
3. G. Nootz, E. Jarosz, F. R. Dalgleish, and W. Hou, "Quantification of optical turbulence in the ocean and its effects on beam propagation," *Appl. Opt.* **55**, 8813–8820 (2016).
4. S. Avramov-Zamurovic, A. T. Watnik, J. R. Lindle, K. P. Judd, and J. M. Esposito, "Machine learning-aided classification of beams carrying orbital angular momentum propagated in highly turbid water," *J. Opt. Soc. Am. A* **37**, 1662–1672 (2020).

5. S. R. Park, L. Cattell, J. M. Nichols, A. Watnik, T. Doster, and G. K. Rohde, "De-multiplexing vortex modes in optical communications using transport-based pattern recognition," *Opt. Express* **26**, 4004–4022 (2018).
6. W. A. Jarrett, S. Avramov-Zamurovic, and J. M. Esposito, "Experimental evaluation of the impact of physical beam misalignment on the performance of an underwater wireless optical communication network utilizing machine learning," *Opt. Commun.* **529**, 129069 (2023).
7. S. Avramov-Zamurovic, A. T. Watnik, J. R. Lindle, and K. P. Judd, "Designing laser beams carrying OAM for a high-performance underwater communication system," *J. Opt. Soc. Am. A* **37**, 876–887 (2020).
8. R. B. Holmes, "Adaptive optics for directed energy: fundamentals and methodology," *AIAA J.* **60**, 5633–5644 (2022).
9. M. Kalensky, M. F. Spencer, E. J. Jumper, and S. Gordeyev, "Estimation of atmospheric optical turbulence strength in realistic airborne environments," *Appl. Opt.* **61**, 6268–6279 (2022).
10. R. J. Hill, "Models of the scalar spectrum for turbulent advection," *J. Fluid Mech.* **88**, 541–562 (1978).
11. R. Antonia and P. Orlandi, "Effect of Schmidt number on small-scale passive scalar turbulence," *Appl. Mech. Rev.* **56**, 615–632 (2003).
12. S. Matt, W. Hou, W. Goode, and S. Hellman, "Introducing SITTE: a controlled laboratory setting to study the impact of turbulent fluctuations on light propagation in the underwater environment," *Opt. Express* **25**, 5662–5683 (2017).
13. S. Matt, W. Hou, and W. Goode, "The impact of turbulent fluctuations on light propagation in a controlled environment," *Proc. SPIE* **9111**, 235–245 (2014).
14. S. Gladysz, R. Barros, A. V. Kanaev, and W. Hou, "Characterization of underwater optical turbulence on the example of the Rayleigh-Bénard water tank," *Proc. SPIE* **10425**, 57–65 (2017).
15. G. Nootz, S. Matt, A. Kanaev, K. P. Judd, and W. Hou, "Experimental and numerical study of underwater beam propagation in a Rayleigh-Bénard turbulence tank," *Appl. Opt.* **56**, 6065–6072 (2017).
16. S. Matt, W. Hou, W. Goode, G. Liu, M. Han, A. V. Kanaev, and S. Restaino, "A controlled laboratory environment to study EO signal degradation due to underwater turbulence," *Proc. SPIE* **9459**, 70–79 (2015).
17. A. V. Kanaev, W. Hou, S. R. Restaino, S. Matt, and S. Gladysz, "Restoration of images degraded by underwater turbulence using structure tensor oriented image quality (STOIQ) metric," *Opt. Express* **23**, 17077–17090 (2015).
18. J. P. Montoya, M. Segel, S. Gladysz, M. Kremer, and K. Stein, "Measurements of temperature and image motion structure functions in a Rayleigh-Bénard water tank," in *Imaging and Applied Optics 2019 (COSI, IS, MATH, pcAOP)* (Optica Publishing Group, 2019), paper PTh4C.3.
19. S. Gladysz, M. Segel, J. Montoya, I. Toselli, O. J. Galicia Gasperin, and K. Stein, "Modelling, measurement and correction of underwater turbulence effects on optical communications," in *5th Underwater Communications and Networking Conference (UComms)* (2021), pp. 1–4.
20. K. P. Judd, S. Avramov-Zamurovic, S. Matt, R. A. Handler, A. T. Watnik, J. R. Lindle, J. Esposito, and W. A. Jarrett, "Propagation of laser beams carrying orbital angular momentum through simulated optical turbulence in Rayleigh-Bénard convection," *Proc. SPIE* **11860**, 20–32 (2021).
21. S. Avramov-Zamurovic, C. Nelson, and J. M. Esposito, "Classification of beams carrying orbital angular momentum propagating through underwater turbulence," *Proc. SPIE* **11532**, 48–55 (2020).
22. S. Avramov-Zamurovic, C. Nelson, and J. M. Esposito, "Experimentally evaluating beam scintillation and vortex structure as a function of topological charge in underwater optical turbulence," *Opt. Commun.* **513**, 128079 (2022).
23. W. Hou, S. Woods, E. Jarosz, W. Goode, and A. Weidemann, "Optical turbulence on underwater image degradation in natural environments," *Appl. Opt.* **51**, 2678–2686 (2012).
24. S. Grossmann and D. Lohse, "Scaling in thermal convection: a unifying theory," *J. Fluid Mech.* **407**, 27–56 (2000).
25. S. Grossmann and D. Lohse, "Prandtl and Rayleigh number dependence of the Reynolds number in turbulent thermal convection," *Phys. Rev. E* **66**, 016305 (2002).
26. S. Grossmann and D. Lohse, "On geometry effects in Rayleigh-Bénard convection," *J. Fluid Mech.* **486**, 105–114 (2003).
27. S. Grossmann and D. Lohse, "Fluctuations in turbulent Rayleigh-Bénard convection: The role of plumes," *Phys. Fluids* **16**, 4462–4472 (2004).
28. V. A. Kulikov, M. S. Andreeva, A. V. Koryabin, and V. I. Shmalhausen, "Method of estimation of turbulence characteristic scales," *Appl. Opt.* **51**, 8505–8515 (2012).
29. V. A. Kulikov and V. I. Shmalhausen, "Thread-shaped intensity field after light propagation through the convective cell," *arXiv*, arXiv:1310.5273 (2013).
30. V. V. Nikishov and V. I. Nikishov, "Spectrum of turbulent fluctuations of the sea-water refraction index," *Int. J. Fluid Mech. Res.* **27**, 82–98 (2000).
31. L. C. Andrews and R. L. Phillips, *Laser Beam Propagation through Random Media*, 2nd ed. (SPIE, 2005).
32. E. P. Magee and B. M. Welsh, "Characterization of laboratory-generated turbulence by optical phase measurements," *Opt. Eng.* **33**, 50–61 (1993).
33. H. L. Grant, R. W. Stewart, and A. Moilliet, "Turbulence spectra from a tidal channel," *J. Fluid Mech.* **12**, 241–268 (1962).
34. R. J. Hill and S. F. Clifford, "Modified spectrum of atmospheric temperature fluctuations and its application to optical propagation," *J. Opt. Soc. Am.* **68**, 892–899 (1978).
35. X. Quan and E. S. Fry, "Empirical equation for the index of refraction of seawater," *Appl. Opt.* **34**, 3477–3480 (1995).
36. R. Frehlich, "Laser scintillation measurements of the temperature spectrum in the atmospheric surface layer," *J. Atmos. Sci.* **49**, 1494–1509 (1992).
37. S. A. Thorpe, *The Turbulent Ocean* (Cambridge University, 2005).
38. R. J. Hill, "Optical propagation in turbulent water," *J. Opt. Soc. Am.* **68**, 1067–1072 (1978).
39. V. I. Tatarski, *Wave Propagation in a Turbulent Medium*, reissue edition (Dover, 2016).
40. A. Muschinski and S. M. d. B. Kops, "Investigation of Hill's optical turbulence model by means of direct numerical simulation," *J. Opt. Soc. Am. A* **32**, 2423–2430 (2015).
41. D. Wayne, "Measuring optical turbulence parameters with a three-aperture receiver," Electronic Theses and Dissertations (University of Central Florida, 2006).
42. M. S. Emran and J. Schumacher, "Conditional statistics of thermal dissipation rate in turbulent Rayleigh-Bénard convection," *Eur. Phys. J. E* **35**, 108 (2012).
43. J. D. Schmidt, *Numerical Simulation of Optical Wave Propagation with Examples in MATLAB* (SPIE, 2010).
44. J. A. Fleck, J. R. Morris, and M. D. Feit, "Time-dependent propagation of high energy laser beams through the atmosphere," *Appl. Phys.* **10**, 129–160 (1976).
45. N. A. Ferlic, M. v. Iersel, and C. C. Davis, "Weak turbulence effects on different beams carrying orbital angular momentum," *J. Opt. Soc. Am. A* **38**, 1423–1437 (2021).
46. M. Gauding, M. Bode, Y. Brahami, E. Varea, and L. Danaila, "Self-similarity of turbulent jet flows with internal and external intermittency," *J. Fluid Mech.* **919**, A41 (2021).
47. J. P. Bos, M. C. Roggemann, and V. S. R. Gudimetla, "Anisotropic non-Kolmogorov turbulence phase screens with variable orientation," *Appl. Opt.* **54**, 2039–2045 (2015).
48. J.-R. Yao, J.-R. Yao, H.-T. Wang, H.-J. Zhang, J.-D. Cai, M.-Y. Ren, Y. Zhang, Y. Zhang, and O. Korotkova, "Oceanic non-Kolmogorov optical turbulence and spherical wave propagation," *Opt. Express* **29**, 1340–1359 (2021).
49. V. I. Tatarskii, *The Effects of the Turbulent Atmosphere on Wave Propagation* (Israel Program for Scientific Translations, 1971).
50. C. E. Coulman, J. Vernin, Y. Coqueugniot, and J. L. Caccia, "Outer scale of turbulence appropriate to modeling refractive-index structure profiles," *Appl. Opt.* **27**, 155–160 (1988).